NeuroImage: Clinical 33 (2022) 102890

Contents lists available at ScienceDirect

NeuroImage: Clinical

journal homepage: www.elsevier.com/locate/ynicl

Fast and equilibrium CEST imaging of brain tumor patients at 3T

Yin Wu [a,b,1], Zhou Liu [a,c,1], Qian Yang [c], Liyan Zou [c], Fan Zhang [d], Long Qian [e], Xin Liu [a,b], Hairong Zheng [a,b], Dehong Luo [c], Phillip Zhe Sun [f,*]

[a] Paul C. Lauterbur Research Center for Biomedical Imaging, Shenzhen Institute of Advanced Technology, Chinese Academy of Sciences, Shenzhen, Guangdong, China
[b] Key Laboratory of Health Informatics, Chinese Academy of Sciences, Shenzhen, Guangdong, China
[c] Department of Radiology, National Cancer Center/National Clinical Research Center for Cancer/Cancer Hospital & Shenzhen Hospital, Chinese Academy of Medical Sciences and Peking Union Medical College, Shenzhen, Guangdong, China
[d] Department of Neurosurgery, National Cancer Center/National Clinical Research Center for Cancer/Cancer Hospital & Shenzhen Hospital, Chinese Academy of Medical Sciences and Peking Union Medical College, Shenzhen, Guangdong, China
[e] MR Research, GE Healthcare, Beijing, China
[f] Department of Radiology and Imaging Sciences, Emory University School of Medicine, Atlanta, GA, USA

ARTICLE INFO

Keywords:
Amide proton transfer
Chemical exchange saturation transfer
Quasi-steady-state (QUASS)
Tumor

ABSTRACT

Chemical exchange saturation transfer (CEST) MRI, versatile for detecting endogenous mobile proteins and tissue pH, has proved valuable in tumor imaging. However, CEST MRI scans are often performed under non-equilibrium conditions, which confound tissue characterization. This study proposed a quasi-steady-state (QUASS) CEST MRI algorithm to standardize fast and accurate tumor imaging at 3 T. The CEST signal evolution was modeled by longitudinal relaxation rate during relaxation delay (Td) and spinlock relaxation during RF saturation time (Ts), from which the QUASS CEST effect is derived. Numerical simulation and human MR imaging experiments (7 healthy volunteers and 19 tumor patients) were conducted at 3 T to compare the CEST measurements obtained under two representative experimental conditions. In addition, amide proton transfer (APT), combined magnetization transfer (MT) and nuclear overhauser enhancement (NOE) effects, and direct water saturation were isolated using a 3-pool Lorentzian fitting in white matter and gray matter of healthy volunteers and for patients in the contralateral normal-appearing white matter and tumor regions. Finally, the student's *t*-test was performed between conventional and QUASS CEST measurements. The routine APT and combined MT & NOE measures significantly varied with Ts and Td ($P < .001$) and were significantly smaller than the corresponding QUASS indices ($P < .001$). In contrast, the results from the QUASS reconstruction showed little dependence on the scan protocol ($P > .05$), indicating the accuracy and robustness of QUASS CEST MRI for tumor imaging. To summarize, the QUASS CEST reconstruction algorithm enables fast and accurate tumor CEST imaging at 3 T, promising to expedite and standardize clinical CEST MRI.

1. Introduction

Amide proton transfer (APT) is a specific chemical exchange saturation transfer (CEST) MRI sensitizing to mobile proteins/peptides and tissue pH. It has emerged as a promising non-invasive imaging approach to complement gadolinium-enhanced and perfusion MRI that together characterize not only hemodynamic and blood brain barrier states but also the altered tumor microenvironment. Briefly, the APT signal appears hyperintense in high-grade glioblastoma, while it shows isointense in low-grade glioma as the normal brain tissue (Choi et al., 2017; Park et al., 2016b; Su et al., 2017; Togao et al., 2017; Zhou et al., 2013). Although it has been long recognized that it is not straightforward to differentiate tumor recurrence from treatment necrosis (Verma et al., 2013), APT MRI can distinguish active glioma from radiation effects (Togao et al., 2014; Zhou et al., 2011). As such, APT and variants of CEST MRI have been increasingly adopted for tumor imaging (Jiang et al., 2019; Sagiyama et al., 2014).

Although CEST MRI is versatile, its measurement is highly variable among studies. This is because the CEST measurement depends not only on tissue properties but also on scan parameters (Dula et al., 2015; Kim

* Corresponding author at: Department of Radiology and Imaging Sciences, Emory University School of Medicine, 954 Gatewood Road NE, Atlanta, GA 30329, USA.
E-mail address: pzhesun@emory.edu (P.Z. Sun).
[1] These authors contributed equally to this work.

https://doi.org/10.1016/j.nicl.2021.102890
Received 26 September 2021; Received in revised form 10 November 2021; Accepted 16 November 2021
Available online 27 November 2021

et al., 2015), including the radiofrequency (RF) saturation amplitude, saturation time (Ts), and the relaxation delay (Td) (Sun et al., 2013; Zaiss et al., 2018). Furthermore, whereas quantitative in vivo CEST MRI has progressed substantially, most solutions assumed equilibrium states. To make it more challenging, nearly all CEST scans have been performed under non-equilibrium conditions due to scan time or hardware constraints. Thus, there is an unmet need to standardize the CEST MRI measurements across sites and facilitate its adoption in the clinical setting. Towards this goal, our study herein proposed a quasi-steady-state (QUASS) postprocessing algorithm to reconstruct the equilibrium CEST effect for imaging brain tumor patients at 3 T. Building on numerical simulations, both healthy volunteers and brain tumor patients were enrolled to test the accuracy and reproducibility of QUASS CEST MRI in the clinical setting, demonstrating its advantage for tumor imaging over routine CEST MRI.

2. Materials and methods

2.1. Theory

The spinlock theory provides a simplified quantitative description of CEST MRI measurement (Jiang et al., 2016; Jin et al., 2011; Zaiss and Bachert, 2013). For a representative CEST sequence with a continuous wave RF saturation, the saturated scan (I) under long relaxation delay normalized by respective control scan without RF irradiation (I_0) can be shown as (Jin et al., 2011; Zaiss and Bachert, 2013),

$$\frac{I}{I_0} = e^{-R_{1\rho}\cdot Ts} + \frac{R_{1w}}{R_{1\rho}} cos^2\theta (1 - e^{-R_{1\rho}\cdot Ts}) \quad (1)$$

where R_{1w} is the longitudinal relaxation rate of water and θ is the effective tipping angle of the RF saturation field. When Ts is sufficiently long, Eq. (1) becomes

$$\frac{I}{I_0} = \frac{R_{1w}}{R_{1\rho}} cos^2\theta \quad (2)$$

However, when the conditions of long relaxation delay and saturation time are not met, Eq. (1) is not accurate. Briefly, the control scan (apparent I_0 , I_0^{app}) is given by $I_0^{app} = I_0 \bullet (1 - e^{-R_{1w}\cdot(Ts + Td)})$, from which the thermal equilibrium state I_0 could be derived, being

$$I_0 = \frac{I_0^{app}}{1 - e^{-R_{1w}\cdot(Ts + Td)}} \quad (3)$$

For the saturated scan with given Ts and Td (apparent I, I^{app}), we have,

$$I^{app} = I_0 \bullet \left(1 - e^{-R_{1w}\cdot Td}\right) e^{-R_{1\rho}\cdot Ts} + I_0 \bullet \frac{R_{1w}}{R_{1\rho}} \cos^2\theta \left(1 - e^{-R_{1\rho}\cdot Ts}\right) \quad (4)$$

Combining Eqs. (3) and (4), we have (Jiang et al., 2016),

$$I^{app} = \frac{I_0^{app}}{1 - e^{-R_{1w}\cdot(Ts + Td)}} \left[\left(1 - e^{-R_{1w}\cdot Td}\right) e^{-R_{1\rho}\cdot Ts} + \frac{R_{1w}}{R_{1\rho}} cos^2\theta \left(1 - e^{-R_{1\rho}\cdot Ts}\right)\right] \quad (5)$$

Eq. (5) could be rewritten as,

$$\frac{I^{app} \bullet \left(1 - e^{-R_{1w}\cdot(Ts + Td)}\right)}{I_0^{app} \bullet \left(1 - e^{-R_{1w}\cdot Td}\right)} = 1 - \left(1 - e^{-R_{1\rho}\cdot Ts}\right) + \frac{R_{1w}}{R_{1\rho}} cos^2\theta \frac{\left(1 - e^{-R_{1\rho}\cdot Ts}\right)}{\left(1 - e^{-R_{1w}\cdot Td}\right)}$$

$$= 1 + \left(1 - e^{-R_{1\rho}\cdot Ts}\right)\left(\frac{R_{1w}}{R_{1\rho}} \bullet \frac{\cos^2\theta}{1 - e^{-R_{1w}\cdot Td}} - 1\right) \quad (6)$$

$R_{1\rho}$ can be numerically solved from Eq. (6), and the QUASS CEST effect is calculated as

$$\left(\frac{I}{I_0}\right)^{QUASS} = \frac{R_{1w}}{R_{1\rho}} cos^2\theta \quad (7)$$

which approximates the equilibrium CEST effect in Eq. (2).

2.2. Numerical simulation

The CEST effect was simulated using Bloch McConnell equations in MATLAB 2021a (MathWorks, Natick, MA) with 3-pools of the bulk water (0 ppm), amide protons (3.5 ppm), and semisolid macromolecules (0 ppm) (Woessner et al., 2005). Typical bulk water T_{1w} and T_{2w} of 1.47 s and 71 ms were used, with amide protons T_{1s} and T_{2s} of 1 s and 15 ms, and macromolecules T_{1MT} and T_{2MT} of 1 s and 10 μs (Stanisz et al., 2005). Two representative amide proton fraction ratios of 0.1% and 0.13% were simulated to illustrate a protein level difference, with a representative amide exchange rate of 100 s^{-1}. We had the fraction ratio and exchange rate for semisolid macromolecules being 13.9% and 23 s^{-1}, respectively. CEST Z-spectra were simulated from −5 to 5 ppm with increments of 0.1 ppm for Ts/Td from 1 to 5 s at intervals of 0.5 s, under a representative RF amplitude (B_1) of 1 μT. The CEST effect was calculated using the routine asymmetry analysis. The confidence bounds of Z-sepctra and respective asymmetry spectra from different Ts/Td were compared between apparent and QUASS measurements to evaluate the impact of saturation parameters on CEST MRI.

2.3. Study participants

The study was approved by the local Institutional Review Board. Written informed consents were obtained from all participants prospectively recruited from November 2020 to March 2021. The enrolled participants included 7 healthy volunteers without a history of neurological disorders (40 ± 13 years, 3 Males) and 19 patients (59 ± 10 years, 4 Males) with the following enrollment criteria: (1) brain lesion detected by MRI examination, and (2) brain tumor confirmed with histology, or clinical diagnosis with follow-up.

2.4. MRI study

Participants underwent MR scans with a 24-channel head coil on a 3 T scanner (Discovery MR 750w, General Electric, Waukesha, WI). An inversion recovery T_1-weighted mapping with single-shot fast-spin-echo (FSE) readout was acquired (FOV = 240 × 240 mm^2, in-planar resolution = 1.9 × 1.9 mm^2, slice thickness = 5 mm (single slice), recovery time/TE = 5000/7.7 ms, multiple TI = 200, 500, 800, 1100, and 1400 ms). A rectangular-shaped continuous wave RF saturation pulse was used for CEST MRI. Z-spectra were obtained from −600 to 600 Hz with intervals of 20 Hz under a B_1 of 1 μT. CHEmical Selective Saturation (CHESS) was employed to suppress fat signal followed by single-shot FSE image readout without any accelerated method for data acquisition (TE = 26 ms, echo spacing = 3.6 ms, and readout bandwidth = 976.6 Hz/Pixel) with two representative Ts/Td parameters of 1 s/1s and 2 s/2s, in addition to unsaturated control scans. Their scan times were 2.1 min and 4.3 min for Ts/Td of 1 s/1s and 2 s/2s, respectively. Gadolinium-enhanced T_1w fluid-attenuated inversion recovery imaging was conducted 5 min after intravenous injection of 0.2 mL/kg of the gadolinium contrast agent (Dotarem, Guerbet Inc., France), with imaging parameters of TR/TE = 3000/26 ms, TI = 870 ms, and spatial resolution = 0.75 × 0.75 × 5 mm^3.

2.5. Data analysis

The parametric T_1 map (T_{1w}) was obtained by fitting the signal with respect to the recovery time ($I_i = I_0[1 - (1 - \eta)e^{-TI_i/T_{1w}}]$) per pixel, where η is the inversion efficiency, and TI_i is the i^{th} inversion time (Ji et al., 2021). The saturated scans (I^{app}) were normalized by the control scan (I_0^{app}) without RF saturation (i.e., $Z^{app} = \frac{I^{app}}{I_0^{app}}$). The superscript app denotes that these indices were simply calculated from measured signals. The field inhomogeneity was corrected using the water saturation

shift reference (WASSR) algorithm (Kim et al., 2009). For the QUASS reconstruction, $R_{1\rho}$ was estimated from Eq. (6), from which the QUASS CEST effect was calculated (Eq. (7)). The multipool Z^{app} and Z^{QUASS} were isolated using a 3-pool Lorentzian model, $Z(\omega) = 1 - \sum_{i=1}^{3} L_i(\omega)$, where L_i is the Lorentzian spectrum of the *i*th pool. As magnetization transfer (MT) and the nuclear overhauser enhancement (NOE) effect overlap substantially at 3 T, they were combined as a single component (Zhang et al., 2018). Saturation transfer effects, including APT, combined MT & NOE, and direct water saturation, were resolved, with their chemical shifts at 3.5, −1.5, and 0 ppm, respectively (Wu et al., 2019; Xu et al., 2014; Zhang et al., 2017). For healthy volunteers, skulls and ventricles were excluded, and gray matter (GM) and white matter (WM) were segmented with empirical thresholding of T_1 (WM: $T_{1w} < 1.2$ s, and GM: $1.2\ s < T_{1w} < 2$ s) (Stanisz et al., 2005). Two neuroradiologists reviewed and confirmed the segmentation results. For patients, ROIs were outlined by two neuroradiologists based on Gd-enhanced T_1w and conventional MR images. Any discrepancies were resolved through a consensus discussion. ROIs were placed at the solid portion of tumors and contralateral normal-appearing white matter (CNAWM). Note that necrosis, hemorrhage, and peripheral edema were excluded from the analysis. Apparent and QUASS CEST effects were calculated from Z^{app} and Z^{QUASS}, respectively, in each ROI.

2.6. Statistical analysis

Values were reported as mean ± standard deviation. Paired Student's *t*-test was applied, and P values<0.05 were considered statistically significant.

3. Results

3.1. Numerical simulation data

The dependence of the CEST effect on the saturation time and relaxation delay was illustrated in Fig. 1. The mean Z-spectra were plotted in solid lines for two amide proton concentrations (i.e., *fs* = 0.13% (red) and *fs* = 0.1% (green)) with the ranges of Z-spectra from different Ts/Td marked by the confidence bounds, widespread and substantially overlapped, indicating substantial dependence on saturation parameters (Fig. 1a). Fig. 1b shows the apparent asymmetry spectra. Although the CEST effect increases with the amide concentration, different Ts/Td causes large variance, suggesting that it is challenging to compare routine CEST MRI results unless identical protocols are chosen. Furthermore, for each amide proton concentration, the Z-spectral intensity was higher at shorter Ts/Td times due to insufficient saturation transfer, leading to noticeably smaller CEST effects at 3.5 ppm than that at longer Ts/Td. In comparison, the QUASS algorithm-reconstructed Z-spectra (Fig. 1c) showed substantially narrowed confidence bounds, clearly revealing the concentration difference. Furthermore, despite the considerable range of the simulated Ts and Td, the QUASS asymmetry spectra showed two CEST effects independent of Ts/Td (Fig. 1d). Altogether, the QUASS algorithm suppresses the impact of experimental conditions on the CEST measurement and derives the equilibrium CEST effect from the apparent metrics.

3.2. Demographic information

The enrolled participants included 7 healthy volunteers without a history of any known neurological disorders (3 Males/4 Females) and 19 patients (4 Males/15 Females). Patient demographics are summarized in Table 1. Five patients had primary brain tumors, and the remaining 14 had brain metastases.

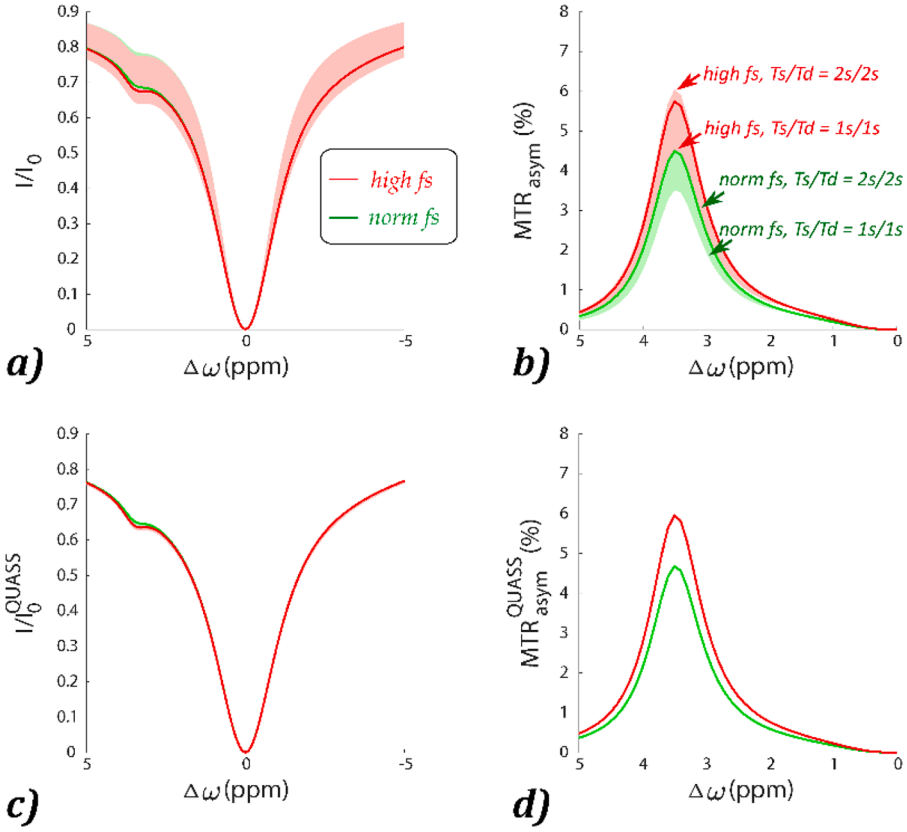

Fig. 1. Simulation of the apparent and QUASS CEST signals under conditions of different saturation time (Ts) and relaxation delay (Td). (a) Apparent Z-spectra for two amide proton fraction ratios obtained for Ts/Td from 1 s to 5 s at intervals of 0.5 s, under a representative RF amplitude (B_1) of 1 μT. The mean Z-spectral signals were plotted in solid lines with their ranges marked by the confidence bounds. (b) The apparent asymmetry spectra. (c) The reconstructed QUASS Z-spectra for the same two amide proton fraction ratios. (d) The QUASS asymmetry spectra.

Table 1
Demographics of enrolled patients.

No.	Age	Gender	Tumor type	Primary tumor	Lesion location within the image plane (lesion No.)	Diagnostic method
1	62	Female	Meningioma	Not applicable	Left frontal lobe (1)	Clinical diagnosis and follow-up
2	64	Female	Metastasis	Lung adenocarcinoma	Left Parietal lobe (1)	Histology
3	58	Female	Metastasis	Lung adenocarcinoma	Right frontal lobe (1)	Clinical diagnosis and follow-up
4	73	Female	Metastasis	Breast cancer	Left Parietal lobe (1)	Clinical diagnosis and follow-up
5	63	Female	Meningioma	Not applicable	Left cavernous sinus (1)	Clinical diagnosis and follow-up
6	55	Female	Metastasis	Lung adenocarcinoma	Left parietal and occipital lobe (1)	Clinical diagnosis and follow-up
7	68	Male	Metastasis	Esophageal carcinoma	Right cerebellum (1)	Histology
8	57	Female	Meningioma	Not applicable	Right parietal lobe (1)	Histology
9	61	Female	Metastasis	Breast cancer	Left parietal lobe (1)	Clinical diagnosis and follow-up
10	62	Male	Metastasis	Lung small cell carcinoma	Left frontal lobe, right centrum semiovale (2)	Clinical diagnosis and follow-up
11	70	Female	Metastasis	Lung adenocarcinoma	Left temporal lobe (1)	Histology
12	57	Female	Metastasis	Breast cancer	Right cerebellum (1)	Clinical diagnosis and follow-up
13	72	Male	Metastasis	Lung cancer	Bilateral parietal lobe and bilateral frontal lobe (4)	Histology
14	62	Female	Metastasis	Lung adenocarcinoma	Left cerebellum (1)	Clinical diagnosis and follow-up
15	69	Female	Metastasis	Lung adenocarcinoma	Left occipital lobe (1)	Histology
16	33	Female	Metastasis	Lung adenocarcinoma	Left fronto-parietal junction (1)	Clinical diagnosis and follow-up
17	43	Female	Metastasis	Breast invasive ductal carcinoma	Left cerebellum (1)	Clinical diagnosis and follow-up
18	58	Female	Meningioma	Not applicable	Pineal area (1)	Clinical diagnosis and follow-up
19	44	Male	Glioblastoma	Not applicable	Bilateral periventricles and splenium of the corpus callosum (2)	Histology

3.3. Healthy volunteer data

Fig. 2 shows two CEST Z-spectra from a region of interest in the WM of a representative healthy volunteer (28 years, Male). The Z-spectrum acquired using short Ts/Td (1 s/1s) was substantially higher than that with the long Ts/Td of 2 s/2s (Fig. 2a), resulting in a difference in resolved CEST effects (Fig. 2b). In comparison, the QUASS Z-spectra (Fig. 2c) were nearly identical for the two sets of Ts/Td parameters. Note that the QUASS Z-spectra were lower than the apparent Z-spectra, suggesting that 2 s was not sufficiently long to obtain the equilibrium state. In addition, QUASS Z-spectra and resolved APT and combined MT & NOE curves overlapped well between different Ts/Td, indicating robust CEST quantification (Fig. 2d).

Fig. 3 shows multiparametric images of a representative healthy volunteer. The histograms show the apparent MT & NOE and APT maps increase with Ts/Td, indicating that the use of short Ts/Td leads to a noticeable underestimation of the CEST effect due to partial saturation transfer. In comparison, QUASS maps were more consistent between different Ts/Td values than the corresponding apparent CEST maps.

3.4. Tumor patient data

Similarly, consistent QUASS CEST MRI results were observed in tumor patients. Fig. 4 shows multiparametric images of a meningioma patient (57 years, Female, Patient No. 8 in Table 1). Compared with the contralateral normal-appearing white matter (CNAWM), the Gd-enhanced tumor region exhibits hyperintensity in T_1 and APT images with a signal decrease in combined MT & NOE maps. The magnitude of

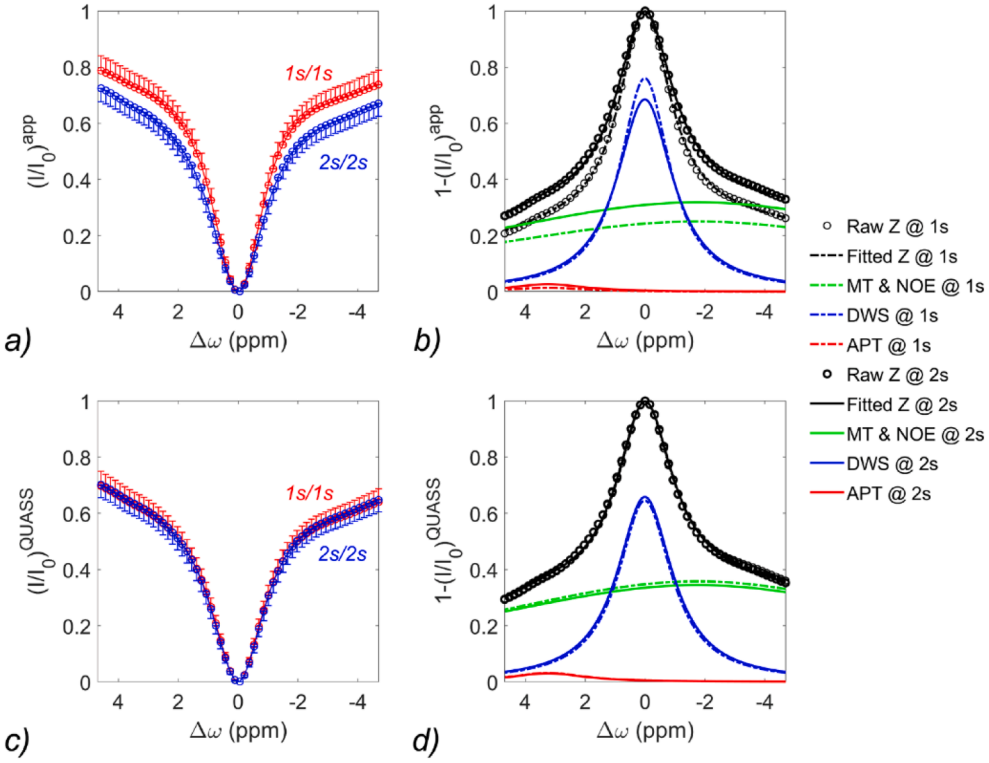

Fig. 2. Comparison of (a) apparent Z-spectra and multipool Lorentzian fitting (b) in white matter (WM) from a 28 years old male volunteer with Ts/Td of 1 s/1s and 2 s/2s, respectively. The corresponding QUASS Z-spectra (c) and multipool Lorentzian fitting (d).

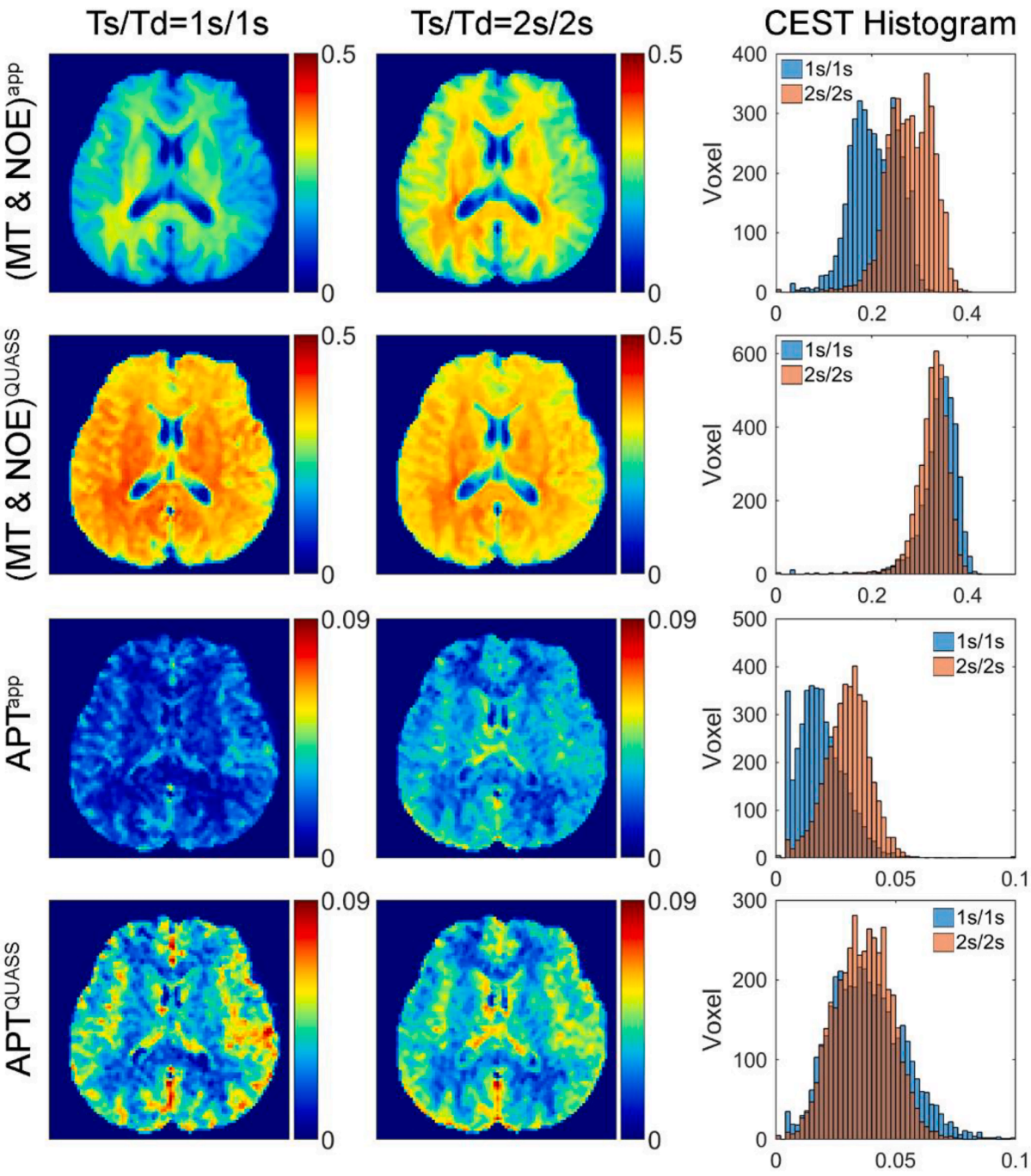

Fig. 3. Multi-parametric MR images of a representative healthy volunteer, including apparent and QUASS CEST maps of combined MT & NOE and APT and their histogram analysis of the whole brain with Ts/Td 1 s/1s and 2 s/2s, respectively.

the apparent CEST effect increased with the Ts/Td. In comparison, QUASS CEST images were substantially stronger than the apparent CEST images. While the apparent APT effect showed little hyperintensity, the QUASS APT displayed a signal increase in the region of Gd enhancement. Multiparametric images of two representative patients with histologically confirmed metastatic brain tumors (patient No.11 in Table 1) and glioblastoma (patient No.19 in Table) were illustrated in Figs. 5 and 6. Similarly, robust QUASS CEST quantification in good agreement with Gd-enhanced tumor was shown in both cases, supported by the histology.

The correlation and consistency of the apparent and QUASS measurements obtained under different Ts/Td were tested. The apparent measurements deviated noticeably from the identity line (Fig. 7a). The Bland-Altman plots showed that apparent APT had a significant shift between different Ts/Td (Fig. 7b). In comparison, the corresponding QUASS measurements were in good agreement (Fig. 7c). Also, Bland-Altman plots showed that QUASS APT exhibited excellent consistency (Fig. 7d) between different Ts/Td. In addition, a better agreement was observed in combined MT & NOE with QUASS measurements than the apparent measures (Fig. 8).

3.5. CEST effect quantification

Table 2 compares the apparent and QUASS CEST measurements under different Ts/Td. For both healthy volunteers (WM and GM) and tumor patients (CNAWM and tumor), the apparent APT and combined

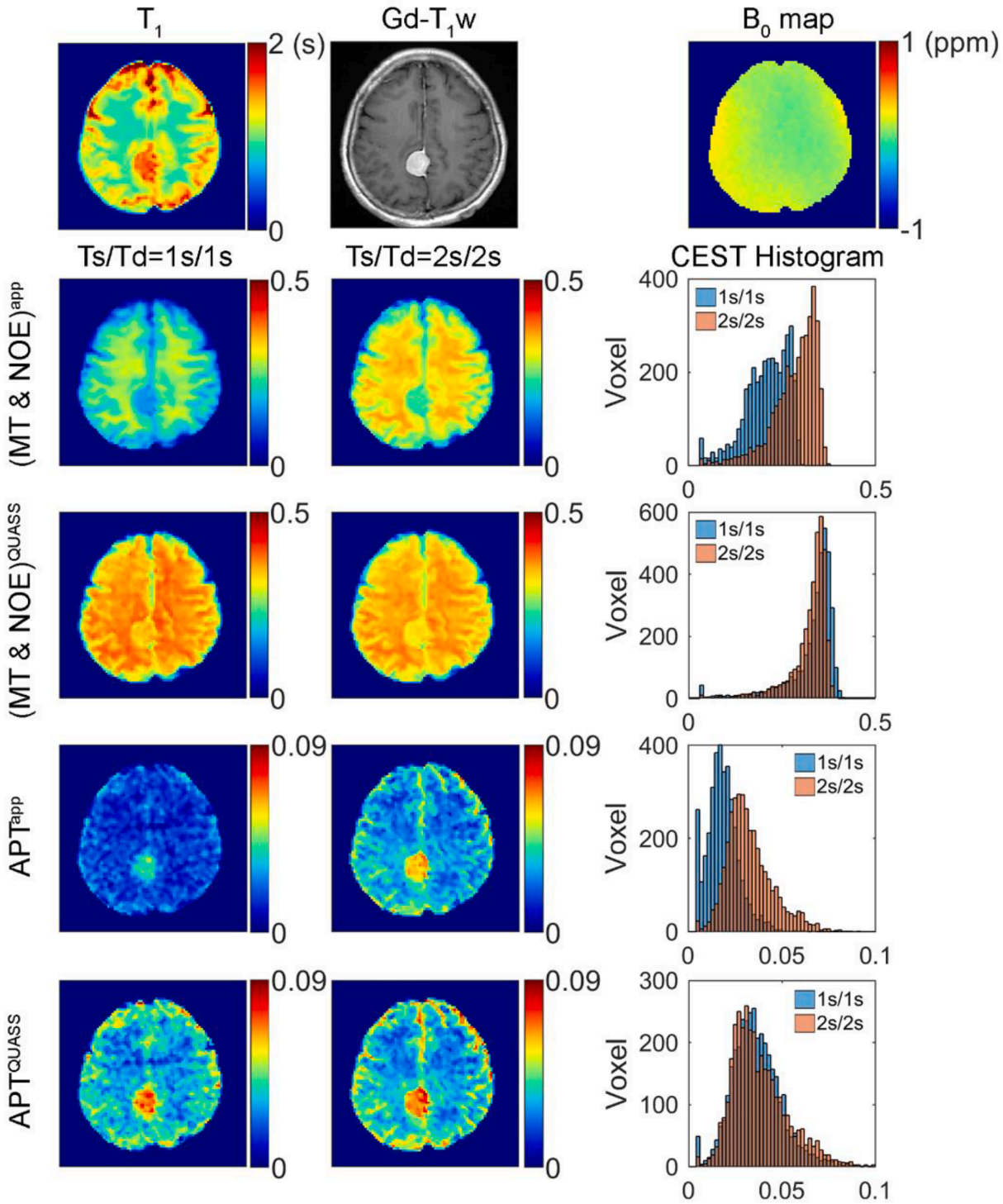

Fig. 4. Multi-parametric MR images of a 57 years old female patient with histologically confirmed meningioma (patient No.8 in Table 1), including T_1 map, Gd enhancement T_1w image, B_0 map, apparent and QUASS CEST maps of combined MT & NOE and APT effects and their histogram analysis of the whole brain with Ts/Td of 1 s/1s and 2 s/2s, respectively.

MT & NOE signals increased significantly with Ts/Td and were significantly lower than respective QUASS measurements ($P < .001$). In comparison, QUASS APT signals were consistently comparable with little dependence on Ts/Td ($P > .05$). Furthermore, although the combined QUASS MT & NOE effects differed significantly between different Ts/Td, the magnitude of the difference was much smaller than the respective apparent measures.

4. Discussion

This study proposed and evaluated the new quasi-steady-state (QUASS) CEST imaging at 3 T. Data from healthy volunteers and brain tumor patients demonstrated that the QUASS algorithm effectively minimizes the impact of experimental conditions on the CEST quantification, promising to expedite CEST clinical examinations without loss in accuracy. In addition, the proposed protocol is uniquely fit to help

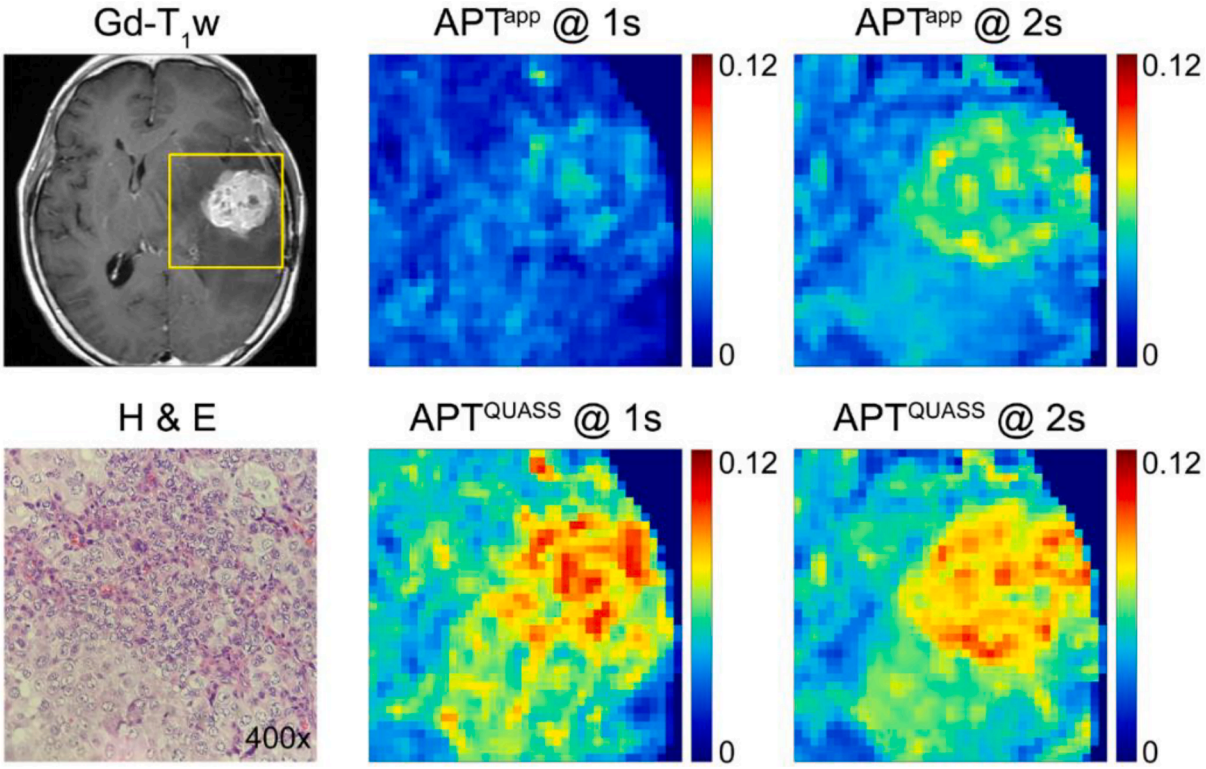

Fig. 5. Multi-parametric MR images of a 70 years old female patient with histologically confirmed metastatic brain tumor (patient No.11 in Table 1), including Gd enhancement T_1w image, apparent and QUASS APT maps with Ts/Td of 1 s/1s and 2 s/2s, respectively.

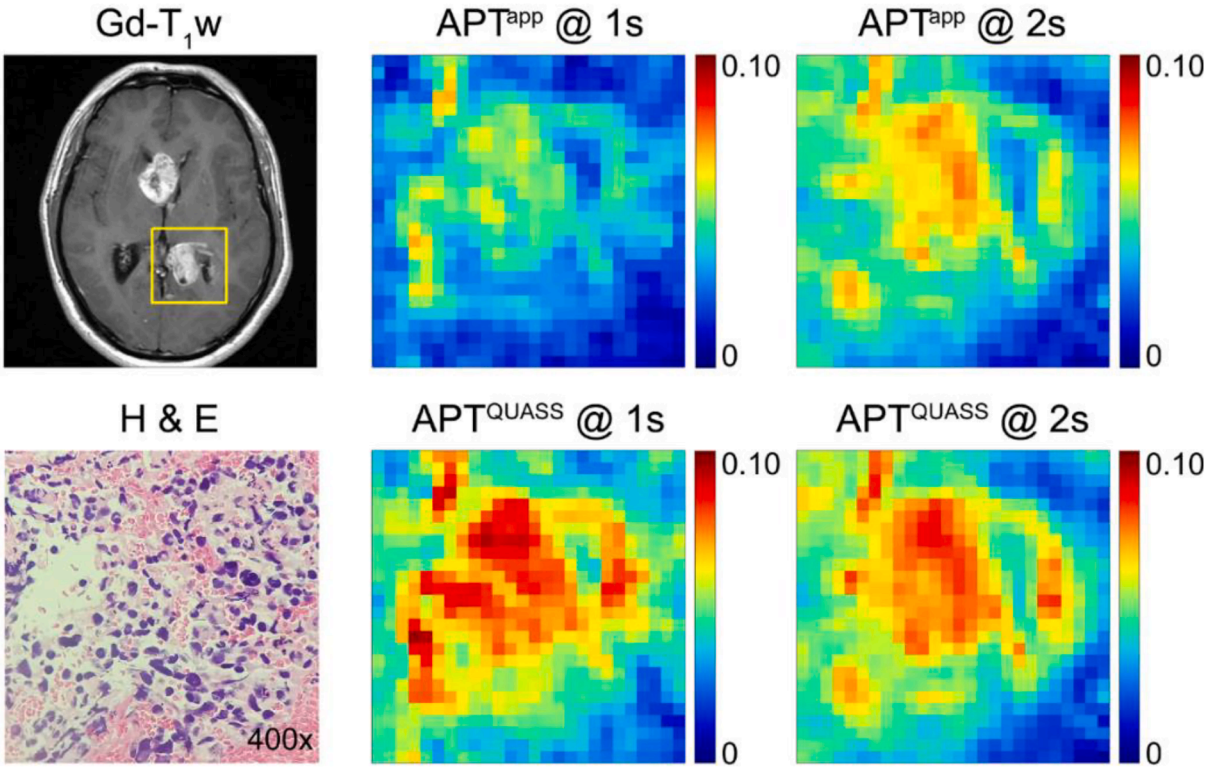

Fig. 6. Multi-parametric MR images of a 44 years old male patient with histologically confirmed glioblastoma (patient No.19 in Table 1), including Gd enhancement T_1w image, apparent and QUASS APT maps with Ts/Td of 1 s/1s and 2 s/2s, respectively.

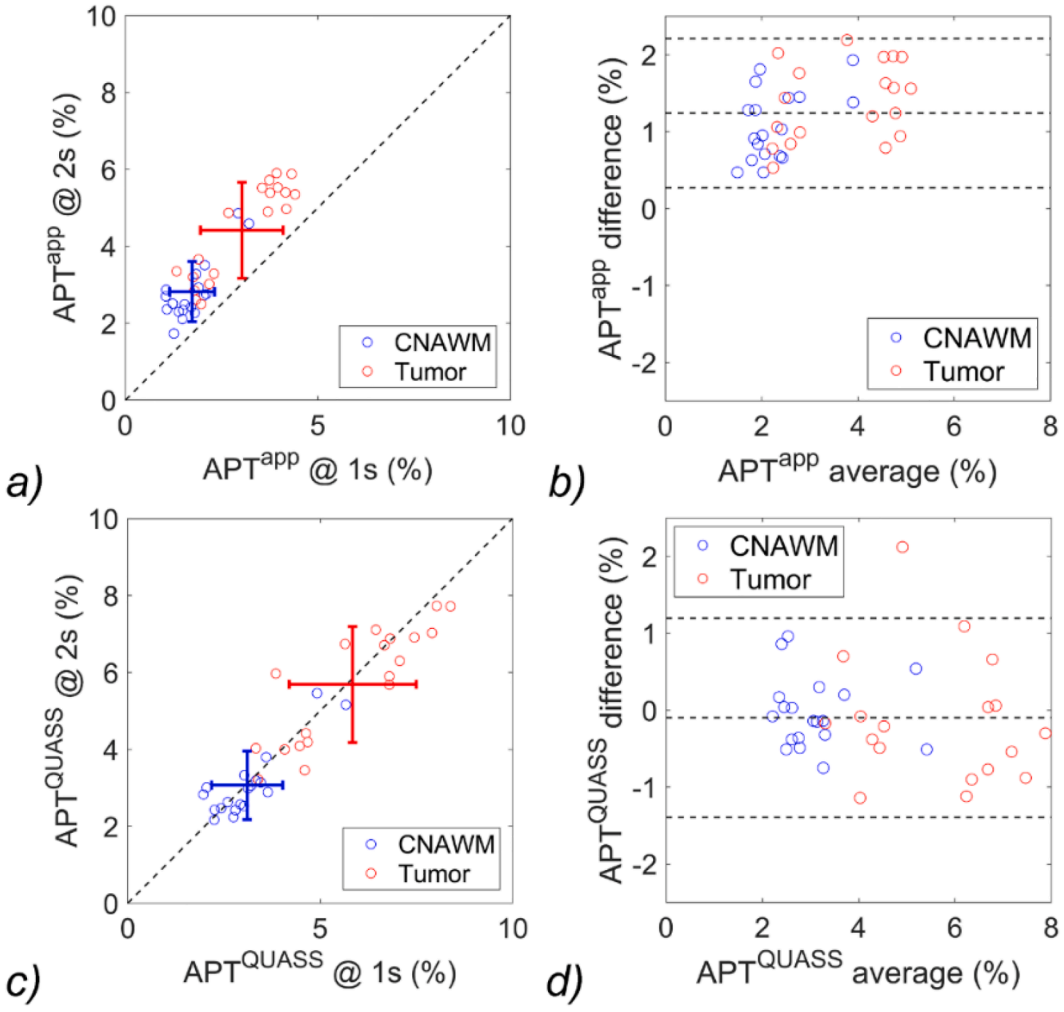

Fig. 7. (a) Correlation test and (b) Bland-Altman plots of the apparent APT measurements, and (c) correlation test and (d) Bland-Altman plots of the QUASS APT measurements between Ts/Td of 2 s/2s and 1 s/1s. The three horizontal lines depict the mean and the upper and lower limits of agreement (i.e., +1.96 and −1.96 times of standard deviation, respectively).

standardized CEST imaging analysis, laying the foundation for elucidation of the complex contrast mechanism of tumor CEST imaging.

We observed a substantial influence of Ts/Td on the apparent APT effect quantification, especially in GM or tumor regions with increased T_1, making them more susceptible to measurement errors than WM or CNAWM. Because long saturation time and relaxation dealy are not commonly used in routine clinical scans due to SAR, hardware, or total scan time limitations, the routine CEST MRI measurement does not yield the equilibrium state. As shown in Table 2, the apparent measures were significantly lower than the reconstructed QUASS MT & NOE and APT effects ($P < .001$), suggesting that even a saturation time of 2 s is not sufficiently long. This likely introduces inaccuracies in downstream CEST quantification, such as the omega plot (Sun, 2021a). Arguably, SNR of CEST MRI scan could be lower when using short Ts/Td. However, the SNR per unit time shall be compared to account for the scan time difference which favors a relatively short Ts/Td (Jiang et al., 2016). As such, the QUASS algorithm allows the scans to be optimized under the peak SNR efficiency condition while reconstructing the equilibrium CEST effect as validated previously (Zhang et al., 2021), promising to advance APT imaging within a shortened scan time and improved SNR efficiency, such as tumor grading and characterization (Jiang et al., 2017; Meissner et al., 2019; Ohno et al., 2016; Park et al., 2016a; Togao et al., 2014; Wu et al., 2019) and pH quantification (Harston et al., 2015; McVicar et al., 2014; Wang et al., 2019a). Also, the QUASS algorithm provides a practical postprocessing approach to standardize the CEST measurements among studies by unifying results obtained from different experimental protocols.

The QUASS algorithm improved the quantification of not only the APT effect but also of the MT & NOE effects. NOE quantification is difficult due to its broad linewidth ranging from 0 to 5 ppm upfield from the water (Mori et al., 1998; van Zijl et al., 2003) and undiscernible peaks from the acquired Z-spectra under the current imaging protocols. Hence, fitting these invisible NOE peaks separately at 3 T could lead to significant errors if the nonlinear DWS and MT contributions are not correctly accounted for. Previous studies have demonstrated decreased NOE and MT effects in tumors compared to normal brain tissues (Cai et al., 2015). Furthermore, the combined MT & NOE effects have shown a negative correlation with Ki-67, an indicator of tumor cell proliferation and growth that differentiates different grades of gliomas (Zhang et al., 2018). Hence, this study chose a previously well-studied model to compare the QUASS and apparent CEST MRI. Our results showed that the tumor regions exhibit significantly reduced combined MT & NOE effects than CNAWM, consistent with previous observations (Wu et al., 2019; Zhang et al., 2018). It could be interesting to further improve the model by isolating MT and NOE contributions in the future and then further apply it to investigate QUASS CEST MRI.

Note that our study did not assume fully relaxed equilibrium magnetization, which is one of the advantages of QUASS reconstruction. Also, our study chose a typical CEST MRI resolution and modeled each voxel as one unit. Admittedly, there could be partial volume within each

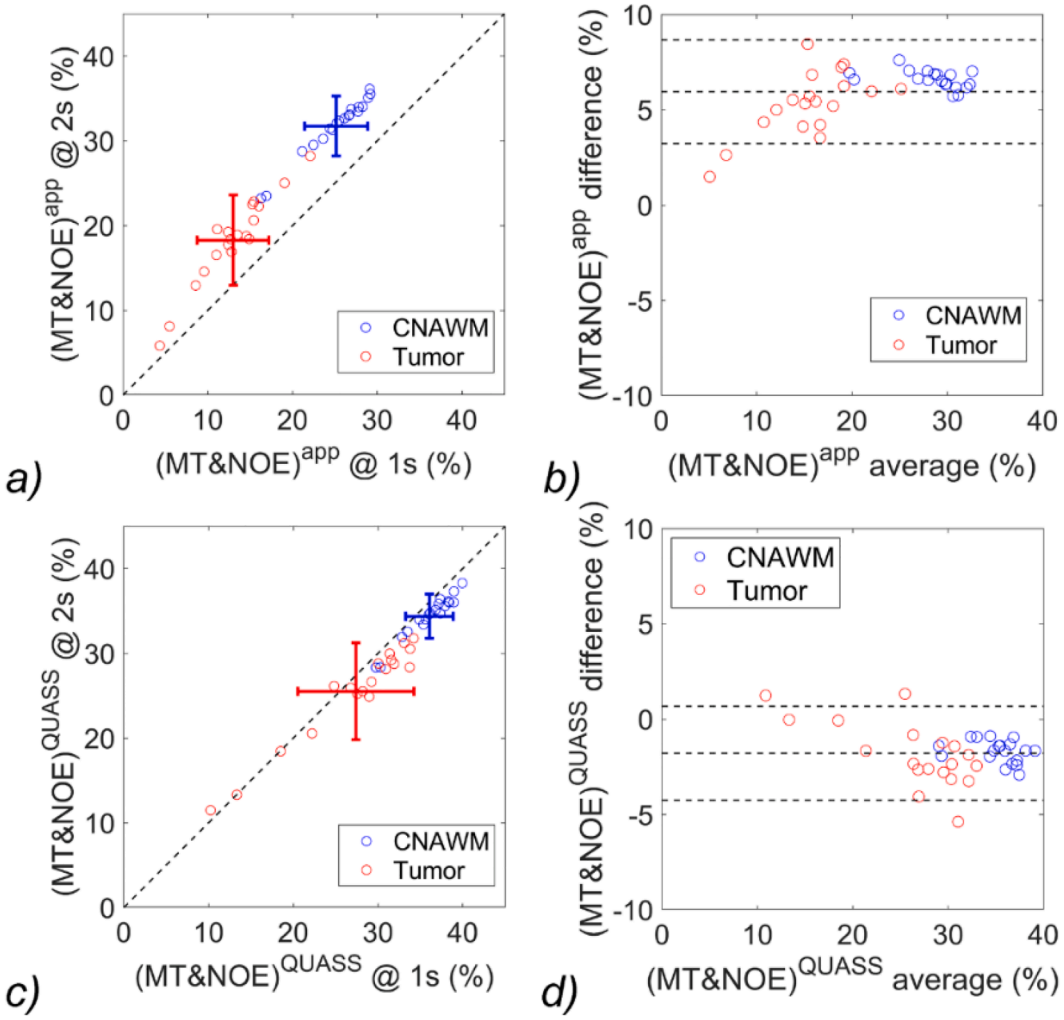

Fig. 8. (a) Correlation test and (b) Bland-Altman plots of the apparent MT & NOE measurements, and (c) correlation test and (d) Bland-Altman plots of the QUASS MT & NOE measurements between Ts/Td of 2 s/2s and 1 s/1s. The three horizontal lines depict the mean and the upper and lower limits of agreement (i.e., +1.96 and −1.96 times of standard deviation, respectively).

Table 2
Comparison of apparent and QUASS CEST effects in white matter (WM) and gray matter (GM) averaged from the 7 healthy volunteers, and in the contralateral normal-appearing white matter (CNAWM) and tumor regions averaged from the 19 patients with saturation time and relaxation delay of 1 s/1s and 2 s/2s

			Apparent			QUASS		
			1 s/1s	2 s/2s	P	1 s/1s	2 s/2s	P
Healthy volunteer	MT & NOE (%)	WM	24.31 ± 0.73	31.42 ± 0.64	<0.001	35.11 ± 1.01	34.05 ± 0.71	<0.001
		GM	18.25 ± 0.83	25.81 ± 1.12	<0.001	33.46 ± 1.17	31.95 ± 1.17	0.002
	APT (%)	WM	1.39 ± 0.19	2.64 ± 0.22	<0.001	2.84 ± 0.18	2.93 ± 0.20	0.106
		GM	1.89 ± 0.23	2.98 ± 0.29	<0.001	3.98 ± 0.36	3.82 ± 0.31	0.154
Patient	MT & NOE (%)	CNAWM	25.14 ± 3.64	31.74 ± 3.43	<0.001	36.08 ± 2.74	34.39 ± 2.55	<0.001
		Tumor	12.99 ± 4.12	18.29 ± 5.20	<0.001	27.40 ± 6.67	25.52 ± 5.57	<0.001
	APT (%)	CNAWM	1.73 ± 0.57	2.82 ± 0.76	<0.001	3.11 ± 0.90	3.07 ± 0.87	0.717
		Tumor	3.02 ± 1.05	4.42 ± 1.21	<0.001	5.85 ± 1.61	5.69 ± 1.46	0.411

voxel, but correcting the intra-voxel partial volume effect is not straightforward. One potential approach will be to collect multi-resolution images to assess the partial volume effect, which could be explored in the future. Nevertheless, both healthy volunteer and tumor patient results showed that the QUASS technique could derive robust CEST measurement with less dependence on Ts/Td, despite the possible partial volume effect.

Most recently, Schüre et al. employed a segmented RF saturation scheme to accelerate CEST MRI (Schüre et al., 2021), building on that proposed by Sun et al. (Sun et al., 2011). Arguably, such an approach only results in steady-state that could differ from the equilibrium state that the QUASS algorithm reconstructs. Therefore, although the current study used the term quai-steady-state as proposed by Sun et al (Sun, 2021b), it should have been the quasi-equilibrium CEST state.

There were several minor limitations of this study that should be noted. First, both primary brain tumor and brain metastasis patients were enrolled. Additionally, most patients had received or were under treatment, including chemotherapy, radiotherapy, and chemo-radiotherapy. Although such heterogeneous enrollment criteria result in elevated variations of routine CEST measurements, the robustness of the

reconstructed QUASS CEST effects demonstrated its feasibility in the clinical setting. Second, the current study used a single-slice CEST MRI sequence, and the adoption of multi-slice or 3D CEST sequences will undoubtedly improve the clinical CEST imaging. A recent study has demonstrated fast multislice QUASS CEST MRI (Kim et al., 2021). Numerical simulation, in-vitro phantom, and healthy subject experiment documented the robust APT measurement over the routine asymmetry analysis when different saturation times and relaxation delays were used. It is critical to investigate its performance in tumor imaging or incorporate the QUASS algorithm into 3D CEST imaging processing (Goerke et al., 2021; Kumar et al., 2021; Mueller et al., 2020) in the future. Third, this study did not consider B_1 inhomogeneity, which has been challenging in clinical CEST imaging. Becaues CEST scans need to be performed under multiple B_1 fields for RF inhomogeneity correction, the scan time would have been substantially prolonged. As such, this study assumed a reasonably B_1 field and did not correct B_1 inhomogeneities. This assumption is likely valid because of the relatively small spatial coverage and the use of a moderate B_1 field. Indeed, no gross CEST MRI inhomogeneity was observed in the intact tissue. Finally, as the QUASS CEST MRI expedites clinical CEST scan without the risk of underestimating the CEST effect, it has the potential to reduce the specific absorption rate via using moderate CEST imaging saturation times. QUASS CEST MRI may be particularly beneficial for applications at high fields where the saturation time needs to be shortened. It would be interesting to investigate other less visible CEST effects (such as guanidinium) at 7 T in future studies (Cai et al., 2012; Ellingson et al., 2019; Harris et al., 2018; Wang et al., 2019b; Yao et al., 2019; Zu et al., 2017).

5. Conclusions

Routine CEST imaging has been performed under non-equilibrium conditions, and hence the experimental conditions confound the measurement. Such a complex dependency hinders the transition of CEST MRI from a research tool to a versatile and quantitative biomarker ready for multi-center experiments. The proposed QUASS CEST protocol addresses this unmet need by minimizing the impact of imaging parameters on CEST quantification. As a result, it not only permits expediting CEST imaging examinations without loss in accuracy, improving the quantitative elucidation of the contrast mechanism, but also makes it more feasible to design multi-center trials and applications.

CRediT authorship contribution statement

Yin Wu: Conceptualization, Methodology, Software, Formal analysis, Investigation, Data curation, Visualization, Writing – original draft, Funding acquisition. **Zhou Liu:** Validation, Formal analysis, Investigation, Data curation, Project administration, Writing – review & editing. **Qian Yang:** Validation, Formal analysis, Investigation. **Liyan Zou:** Formal analysis, Investigation. **Fan Zhang:** Resources. **Long Qian:** Software. **Xin Liu:** Writing – review & editing. **Hairong Zheng:** Writing – review & editing. **Dehong Luo:** Formal analysis, Supervision, Project administration, Writing – review & editing. **Phillip Zhe Sun:** Conceptualization, Methodology, Software, Visualization, Supervision, Writing – review & editing.

Declaration of Competing Interest

The authors declare that they have no known competing financial interests or personal relationships that could have appeared to influence the work reported in this paper.

Acknowledgement

National Natural Science Foundation of China (81871348 and 91859102 to Y.W.) and the Key Areas Research and Development Program of Guangdong (2019B020235001 to Y.W.).

References

Cai, K., Haris, M., Singh, A., Kogan, F., Greenberg, J.H., Hariharan, H., Detre, J.A., Reddy, R., 2012. Magnetic resonance imaging of glutamate. Nat Med 18 (2), 302–306.

Cai, K., Singh, A., Poptani, H., Li, W., Yang, S., Lu, Y., Hariharan, H., Zhou, X.J., Reddy, R., 2015. CEST signal at 2 ppm (CEST@2 ppm) from Z-spectral fitting correlates with creatine distribution in brain tumor. NMR Biomed 28, 1–8.

Choi, Y.S., Ahn, S.S., Lee, S.-K., Chang, J.H., Kang, S.-G., Kim, S.H., Zhou, J., 2017. Amide proton transfer imaging to discriminate between low- and high-grade gliomas: added value to apparent diffusion coefficient and relative cerebral blood volume. Eur Radiol 27 (8), 3181–3189.

Dula, A.N., Dewey, B.E., Arlinghaus, L.R., Williams, J.M., Klomp, D., Yankeelov, T.E., Smith, S., 2015. Optimization of 7-T chemical exchange saturation transfer parameters for validation of glycosaminoglycan and amide proton transfer of fibroglandular breast tissue. Radiology 275 (1), 255–261.

Ellingson, B.M., Yao, J., Raymond, C., Chakhoyan, A., Khatibi, K., Salamon, N., Villablanca, J.P., Wanner, I., Real, C.R., Laiwalla, A., McArthur, D.L., Monti, M.M., Hovda, D.A., Vespa, P.M., 2019. pH-weighted molecular MRI in human traumatic brain injury (TBI) using amine proton chemical exchange saturation transfer echoplanar imaging (CEST EPI). Neuroimage Clin 22, 101736. https://doi.org/10.1016/j.nicl.2019.101736.

Goerke, S., Breitling, J., Korzowski, A., Paech, D., Zaiss, M., Schlemmer, H.-P., Ladd, M. E., Bachert, P., 2021. Clinical routine acquisition protocol for 3D relaxation-compensated APT and rNOE CEST-MRI of the human brain at 3T. Magn Reson Med 86 (1), 393–404.

Harris, R.J., Yao, J., Chakhoyan, A., Raymond, C., Leu, K., Liau, L.M., Nghiemphu, P.L., Lai, A., Salamon, N., Pope, W.B., Cloughesy, T.F., Ellingson, B.M., 2018. Simultaneous pH-sensitive and oxygen-sensitive MRI of human gliomas at 3 T using multi-echo amine proton chemical exchange saturation transfer spin-and-gradient echo echo-planar imaging (CEST-SAGE-EPI). Magn Reson Med 80, 1962–1978.

G.W.J. Harston Y.K. Tee N. Blockley T.W. Okell S. Thandeswaran G. Shaya F. Sheerin M. Cellerini S. Payne P. Jezzard M. Chappell J. Kennedy Identifying the ischaemic penumbra using pH-weighted magnetic resonance imaging 138 1 2015 2015 36 42.

Ji, Y., Lu, D., Jiang, Y., Wang, X., Meng, Y., Sun, P.Z., 2021. Development of fast multi-slice apparent T(1) mapping for improved arterial spin labeling MRI measurement of cerebral blood flow. Magn Reson Med 85 (3), 1571–1580.

Jiang, S., Eberhart, C.G., Lim, M., Heo, H.-Y., Zhang, Y.i., Blair, L., Wen, Z., Holdhoff, M., Lin, D., Huang, P., Qin, H., Quinones-Hinojosa, A., Weingart, J.D., Barker, P.B., Pomper, M.G., Laterra, J., van Zijl, P.C.M., Blakeley, J.O., Zhou, J., 2019. Identifying Recurrent Malignant Glioma after Treatment Using Amide Proton Transfer-Weighted MR Imaging: A Validation Study with Image-Guided Stereotactic Biopsy. Clin Cancer Res 25 (2), 552–561.

Jiang, S., Eberhart, C.G., Zhang, Y.i., Heo, H.-Y., Wen, Z., Blair, L., Qin, H., Lim, M., Quinones-Hinojosa, A., Weingart, J.D., Barker, P.B., Pomper, M.G., Laterra, J., van Zijl, P.C.M., Blakeley, J.O., Zhou, J., 2017. Amide proton transfer-weighted magnetic resonance image-guided stereotactic biopsy in patients with newly diagnosed gliomas. Eur J Cancer 83, 9–18.

Jiang, W., Zhou, I.Y., Wen, L., Zhou, X., Sun, P.Z., 2016. A theoretical analysis of chemical exchange saturation transfer echo planar imaging (CEST-EPI) steady state solution and the CEST sensitivity efficiency-based optimization approach. Contrast Media & Molecular Imaging 11 (5), 415–423.

Jin, T., Autio, J., Obata, T., Kim, S.-G., 2011. Spin-locking versus chemical exchange saturation transfer MRI for investigating chemical exchange process between water and labile metabolite protons. Magnetic Resonance in Medicine 65 (5), 1448–1460.

Kim, H., Krishnamurthy, L.C., Sun, P.Z., 2021. Demonstration of fast multi-slice quasi-steady-state chemical exchange saturation transfer (QUASS CEST) human brain imaging at 3T. Magn Reson Med.

Kim, J., Wu, Y., Guo, Y., Zheng, H., Sun, P.Z., 2015. A review of optimization and quantification techniques for chemical exchange saturation transfer MRI toward sensitive in vivo imaging. Contrast Media & Molecular Imaging 10 (3), 163–178.

Kim, M., Gillen, J., Landman, B.A., Zhou, J., van Zijl, P.C.M., 2009. Water saturation shift referencing (WASSR) for chemical exchange saturation transfer (CEST) experiments. Magn Reson Med 61 (6), 1441–1450.

Kumar, D., Nanga, R.P.R., Thakuri, D., Wilson, N., Cember, A., Martin, M.L., Zhu, D., Shinohara, R.T., Qin, Q., Hariharan, H., Reddy, R., 2021. Recovery kinetics of creatine in mild plantar flexion exercise using 3D creatine CEST imaging at 7 Tesla. Magn Reson Med 85 (2), 802–817.

McVicar, N., Li, A.X., Gonçalves, D.F., Bellyou, M., Meakin, S.O., Prado, M.AM., Bartha, R., 2014. Quantitative tissue pH measurement during cerebral ischemia using amine and amide concentration-independent detection (AACID) with MRI. J Cereb Blood Flow Metab 34 (4), 690–698.

Meissner, J.-E., Korzowski, A., Regnery, S., Goerke, S., Breitling, J., Floca, R.O., Debus, J., Schlemmer, H.-P., Ladd, M.E., Bachert, P., Adeberg, S., Paech, D., 2019. Early response assessment of glioma patients to definitive chemoradiotherapy using chemical exchange saturation transfer imaging at 7 T. J Magn Reson Imaging 50 (4), 1268–1277.

Mori, S., Eleff, S.M., Pilatus, U., Mori, N., van Zijl, P.C.M., 1998. Proton NMR spectroscopy of solvent-saturable resonances: A new approach to study pH effects in Situ. Magn Reson Med 40 (1), 36–42.

Mueller, S., Stirnberg, R., Akbey, S., Ehses, P., Scheffler, K., Stöcker, T., Zaiss, M., 2020. Whole brain snapshot CEST at 3T using 3D-EPI: Aiming for speed, volume, and homogeneity. Magn Reson Med 84 (5), 2469–2483.

Ohno, Y., Yui, M., Koyama, H., Yoshikawa, T., Seki, S., Ueno, Y., Miyazaki, M., Ouyang, C., Sugimura, K., 2016. Chemical Exchange Saturation Transfer MR Imaging: Preliminary Results for Differentiation of Malignant and Benign Thoracic Lesions. Radiology 279 (2), 578–589.

Park, J.E., Kim, H.S., Park, K.J., Kim, S.J., Kim, J.H., Smith, S.A., 2016a. Pre- and Posttreatment Glioma: Comparison of Amide Proton Transfer Imaging with MR Spectroscopy for Biomarkers of Tumor Proliferation. Radiology 278 (2), 514–523.

Park, K.J., Kim, H.S., Park, J.E., Shim, W.H., Kim, S.J., Smith, S.A., 2016b. Added value of amide proton transfer imaging to conventional and perfusion MR imaging for evaluating the treatment response of newly diagnosed glioblastoma. European Radiology 26 (12), 4390–4403.

Sagiyama, K., Mashimo, T., Togao, O., Vemireddy, V., Hatanpaa, K.J., Maher, E.A., Mickey, B.E., Pan, E., Sherry, A.D., Bachoo, R.M., Takahashi, M., 2014. In vivo chemical exchange saturation transfer imaging allows early detection of a therapeutic response in glioblastoma. Proc Natl Acad Sci U S A 111 (12), 4542–4547.

Schüre, J.-R., Pilatus, U., Deichmann, R., Hattingen, E., Shrestha, M., 2021. A fast and novel method for amide proton transfer-chemical exchange saturation transfer multislice imaging. NMR Biomed 34 (7). https://doi.org/10.1002/nbm.v34.710.1002/nbm.4524.

Stanisz, G.J., Odrobina, E.E., Pun, J., Escaravage, M., Graham, S.J., Bronskill, M.J., Henkelman, R.M., 2005. T1, T2 relaxation and magnetization transfer in tissue at 3T. Magn Reson Med 54 (3), 507–512.

Su, C., Liu, C., Zhao, L., Jiang, J., Zhang, J., Li, S., Zhu, W., Wang, J., 2017. Amide Proton Transfer Imaging Allows Detection of Glioma Grades and Tumor Proliferation: Comparison with Ki-67 Expression and Proton MR Spectroscopy Imaging. American Journal of Neuroradiology 38 (9), 1702–1709.

Sun, P.Z., 2021a. Quasi-steady-state CEST (QUASS CEST) solution improves the accuracy of CEST quantification: QUASS CEST MRI-based omega plot analysis. Magn Reson Med 86 (2), 765–776.

Sun, P.Z., 2021b. Quasi-steady state chemical exchange saturation transfer (QUASS CEST) analysis-correction of the finite relaxation delay and saturation time for robust CEST measurement. Magnetic Resonance in Medicine 85 (6), 3281–3289.

Sun, P.Z., Cheung, J.S., Wang, E., Benner, T., Sorensen, A.G., 2011. Fast multislice pH-weighted chemical exchange saturation transfer (CEST) MRI with Unevenly segmented RF irradiation. Magnetic Resonance in Medicine 65 (2), 588–594.

Sun, P.Z., Lu, J., Wu, Y., Xiao, G., Wu, R., 2013. Evaluation of the dependence of CEST-EPI measurement on repetition time, RF irradiation duty cycle and imaging flip angle for enhanced pH sensitivity. Phys Med Biol 58 (17), N229–N240.

Togao, O., Hiwatashi, A., Yamashita, K., Kikuchi, K., Keupp, J., Yoshimoto, K., Kuga, D., Yoneyama, M., Suzuki, S.O., Iwaki, T., Takahashi, M., Iihara, K., Honda, H., 2017. Grading diffuse gliomas without intense contrast enhancement by amide proton transfer MR imaging: comparisons with diffusion- and perfusion-weighted imaging. Eur Radiol 27 (2), 578–588.

Togao, O., Yoshiura, T., Keupp, J., Hiwatashi, A., Yamashita, K., Kikuchi, K., Suzuki, Y., Suzuki, S.O., Iwaki, T., Hata, N., Mizoguchi, M., Yoshimoto, K., Sagiyama, K., Takahashi, M., Honda, H., 2014. Amide proton transfer imaging of adult diffuse gliomas: correlation with histopathological grades. Neuro Oncol 16 (3), 441–448.

van Zijl, P.C.M., Zhou, J., Mori, N., Payen, J.-F., Wilson, D., Mori, S., 2003. Mechanism of magnetization transfer during on-resonance water saturation. a new approach to detect mobile proteins, peptides, and lipids. Magn Reson Med 49 (3), 440–449.

N. Verma M.C. Cowperthwaite M.G. Burnett M.K. Markey Differentiating tumor recurrence from treatment necrosis: a review of neuro-oncologic imaging strategies 15 5 2013 2013 515 534.

Wang, E., Wu, Y., Cheung, J.S., Igarashi, T., Wu, L., Zhang, X., Sun, P.Z., 2019a. Mapping tissue pH in an experimental model of acute stroke - Determination of graded regional tissue pH changes with non-invasive quantitative amide proton transfer MRI. NeuroImage 191, 610–617.

Wang, Y.-L., Yao, J., Chakhoyan, A., Raymond, C., Salamon, N., Liau, L.M., Nghiemphu, P.L., Lai, A., Pope, W.B., Nguyen, N., Ji, M., Cloughesy, T.F., Ellingson, B.M., 2019b. Association between Tumor Acidity and Hypervascularity in Human Gliomas Using pH-Weighted Amine Chemical Exchange Saturation Transfer Echo-Planar Imaging and Dynamic Susceptibility Contrast Perfusion MRI at 3T. AJNR Am J Neuroradiol 40 (6), 979–986.

Woessner, D.E., Zhang, S., Merritt, M.E., Sherry, A.D., 2005. Numerical solution of the Bloch equations provides insights into the optimum design of PARACEST agents for MRI. Magn Reson Med 53 (4), 790–799.

Wu, Y., Chen, Y., Zhao, Y., Yang, S., Zhao, J., Zhou, J., Chen, Z., Sun, P.Z., Zheng, H., 2019. Direct radiofrequency saturation corrected amide proton transfer tumor MRI at 3T. Magn Reson Med 81 (4), 2710–2719.

Xu, J., Zaiss, M., Zu, Z., Li, H., Xie, J., Gochberg, D.F., Bachert, P., Gore, J.C., 2014. On the origins of chemical exchange saturation transfer (CEST) contrast in tumors at 9.4 T. NMR Biomed 27, 406–416.

Yao, J., Tan, C.H.P., Schlossman, J., Chakhoyan, A., Raymond, C., Pope, W.B., Salamon, N., Lai, A., Ji, M., Nghiemphu, P.L., Liau, L.M., Cloughesy, T.F., Ellingson, B.M., 2019. pH-weighted amine chemical exchange saturation transfer echoplanar imaging (CEST-EPI) as a potential early biomarker for bevacizumab failure in recurrent glioblastoma. J Neurooncol 142 (3), 587–595.

Zaiss, M., Angelovski, G., Demetriou, E., McMahon, M.T., Golay, X., Scheffler, K., 2018. QUESP and QUEST revisited - fast and accurate quantitative CEST experiments. Magnetic Resonance in Medicine 79 (3), 1708–1721.

Zaiss, M., Bachert, P., 2013. Exchange-dependent relaxation in the rotating frame for slow and intermediate exchange – modeling off-resonant spin-lock and chemical exchange saturation transfer. NMR Biomed 26 (5), 507–518.

Zhang, J., Zhu, W., Tain, R., Zhou, X.J., Cai, K., 2018. Improved Differentiation of Low-Grade and High-Grade Gliomas and Detection of Tumor Proliferation Using APT Contrast Fitted from Z-Spectrum. Mol Imaging Biol 20 (4), 623–631.

X.-Y. Zhang F. Wang H. Li J. Xu D.F. Gochberg J.C. Gore Z. Zu Accuracy in the quantification of chemical exchange saturation transfer (CEST) 30 7 2017 e3716 10.1002/nbm.v30.7 10.1002/nbm.3716.

Zhang, X.-Y., Zhai, Y., Jin, Z., Li, C., Sun, P.Z., Wu, Y., 2021. Preliminary demonstration of in vivo quasi-steady-state CEST postprocessing-Correction of saturation time and relaxation delay for robust quantification of tumor MT and APT effects. Magn Reson Med 86 (2), 943–953.

Zhou, J., Tryggestad, E., Wen, Z., Lal, B., Zhou, T., Grossman, R., Wang, S., Yan, K., Fu, D.-X., Ford, E., Tyler, B., Blakeley, J., Laterra, J., van Zijl, P.C.M., 2011. Differentiation between glioma and radiation necrosis using molecular magnetic resonance imaging of endogenous proteins and peptides. Nat Med 17 (1), 130–134.

Zhou, J., Zhu, H.e., Lim, M., Blair, L., Quinones-Hinojosa, A., Messina, S.A., Eberhart, C. G., Pomper, M.G., Laterra, J., Barker, P.B., van Zijl, P.C.M., Blakeley, J.O., 2013. Three-dimensional amide proton transfer MR imaging of gliomas: Initial experience and comparison with gadolinium enhancement. Journal of Magnetic Resonance Imaging 38 (5), 1119–1128.

Zu, Z., Louie, E.A., Lin, E.C., Jiang, X., Does, M.D., Gore, J.C., Gochberg, D.F., 2017. Chemical exchange rotation transfer imaging of intermediate-exchanging amines at 2 ppm. NMR Biomed 30.